Journal of Molecular and Cellular Cardiology 166 (2022) 116–126

Contents lists available at ScienceDirect

Journal of Molecular and Cellular Cardiology

journal homepage: www.elsevier.com/locate/yjmcc

Human cardiac myosin-binding protein C phosphorylation- and mutation-dependent structural dynamics monitored by time-resolved FRET

Rhye-Samuel Kanassatega, Thomas A. Bunch, Victoria C. Lepak, Christopher Wang, Brett A. Colson *

Department of Cellular and Molecular Medicine, University of Arizona, Tucson, AZ 85724, United States of America

ARTICLE INFO

Keywords:
Cardiac myosin-binding protein C (cMyBP-C)
Biosensor
Phosphorylation
Protein kinase A (PKA)
Fluorescence lifetime
High-throughput screening (HTS)
Time-resolved fluorescence resonance energy transfer (TR-FRET)

ABSTRACT

Cardiac myosin-binding protein C (cMyBP-C) is a thick filament-associated protein of the sarcomere and a potential therapeutic target for treating contractile dysfunction in heart failure. Mimicking the structural dynamics of phosphorylated cMyBP-C by small-molecule drug binding could lead to therapies that modulate cMyBP-C conformational states, and thereby function, to improve contractility. We have developed a human cMyBP-C biosensor capable of detecting intramolecular structural changes due to phosphorylation and mutation. Using site-directed mutagenesis and time-resolved fluorescence resonance energy transfer (TR-FRET), we substituted cysteines in cMyBP-C N-terminal domains C0 through C2 (C0-C2) for thiol-reactive fluorescent probe labeling to examine C0-C2 structure. We identified a cysteine pair that upon donor-acceptor labeling reports phosphorylation-sensitive structural changes between the C1 domain and the tri-helix bundle of the M-domain that links C1 to C2. Phosphorylation reduced FRET efficiency by ~18%, corresponding to a ~11% increase in the distance between probes and a ~30% increase in disorder between them. The magnitude and precision of phosphorylation-mediated TR-FRET changes, as quantified by the *Z'*-factor, demonstrate the assay's potential for structure-based high-throughput screening of compounds for cMyBP-C-targeted therapies to improve cardiac performance in heart failure. Additionally, by probing C1's spatial positioning relative to the tri-helix bundle, these findings provide new molecular insight into the structural dynamics of phosphoregulation as well as mutations in cMyBP-C. Biosensor sensitivity to disease-relevant mutations in C0-C2 was demonstrated by examination of the hypertrophic cardiomyopathy mutation R282W. The results presented here support a screening platform to identify small molecules that regulate N-terminal cMyBP-C conformational states.

1. Introduction

Cardiac myosin-binding protein C (cMyBP-C) is the most commonly mutated gene associated with hypertrophic cardiomyopathy (HCM), which can also lead to heart failure (HF). HF, most commonly caused by coronary artery disease, high blood pressure, and previous heart attack, is frequently associated with dysregulated cMyBP-C phosphorylation. Thus, cMyBP-C is a prime target for compounds that upon binding restore its function to treat HF and HCM. cMyBP-C is a sarcomeric protein found in 9 axial stripes, spaced ~43 nm apart due to interactions with titin and myosin in the C-zone of the A-band (Fig. 1A) [1–3]. Structurally, cMyBP-C is a ~140 kDa protein consisting of 8 IgI-like and 3 fibronectin-type III domains, referred to as C0-C10 (Fig. 1B) [4–6]. The C-terminal portion (C8-C10) is bound to the myosin-containing thick filaments due to strong interactions with myosin [6–8] and weaker interactions with titin [9,10]. The N-terminal portion (C0-C2) (Fig. 1C) extends away from the thick filament backbone [11,12] towards potential interactions with subfragment-2 (S2) [13] and the regulatory

Abbreviations: cMyBP-C, Cardiac myosin-binding protein C; C0-C2, cMyBP-C N-terminal domains/portion C0 through C2; TR-FRET, time-resolved fluorescence resonance energy transfer; HCM, hypertrophic cardiomyopathy; HF, heart failure; S2, myosin subfragment-2; RLC, myosin regulatory light chain; P/A, proline/alanine-rich linker; Tm, tropomyosin; cTnI, cardiac troponin-I; M-domain, motif domain; IAEDANS, (5-((((2-Iodoacetyl)amino)ethyl)amino)Naphthalene-1-Sulfonic acid; DDPM, N-(4-(dimethylamino)-3,5-dinitrophenyl)maleimide; FLTPR, fluorescence lifetime plate reader; HTS, high-throughput screening; TCEP, tris(2-carboxyethyl)phosphine; DTT, dithiothreitol; CD, circular dichroism; IRF, instrument response function; D_{only}, donor-only; D-A, donor-acceptor; FWHM, full width at half-maximum; MRE, molar residue ellipticity; C0-C2$^{Cys225.Cys330}$, biosensor.

* Corresponding author.
E-mail address: bcolson@arizona.edu (B.A. Colson).

https://doi.org/10.1016/j.yjmcc.2022.02.005
Received 11 September 2021; Received in revised form 31 January 2022; Accepted 21 February 2022
Available online 25 February 2022

light chain (RLC) [14] of myosin, actin, and tropomyosin (Tm) of the thin filament [15–17]. These interactions with the thick and thin filaments are thought to regulate contractile function.

The activation of the β-adrenergic signaling pathway leads to phosphorylation of sarcomeric proteins to accelerate cardiac muscle contraction and relaxation kinetics. The phosphorylation of cMyBP-C contributes to proper diastolic function [18] and responsiveness to β-adrenergic activation, leading to increased contractility and cardiac output by regulating actin-myosin interactions [5,19–22]. At low Ca^{2+} levels, cMyBP-C can activate thin filaments by interactions with actin-Tm [16], but at high Ca^{2+}, cMyBP-C could play an inhibitory role on the actin-myosin interaction [23]. Upon β-adrenergic stimulation, protein kinase A (PKA) phosphorylates cMyBP-C [24] in the M-domain (connecting C1 to C2, Fig. 1B-D), which results in a marked reduction in the binding of N-terminal cMyBP-C to actin and myosin filaments [13,25–27]. This phosphorylation of cMyBP-C, as well as cardiac troponin-I (cTnI) [21] and titin [28], modulates cardiac performance via β-adrenergic signaling on a beat-to-beat basis in healthy myocardium.

In studies of healthy human donor hearts, cMyBP-C is highly phosphorylated at four serines in the M-domain (Fig. 1B, C, E) [29,30]. In contrast, patients diagnosed with HF and comorbidities that lead to HF (e.g., chronic atrial fibrillation and hypertrophic cardiomyopathy) show ~40–75% reduction in total cMyBP-C phosphorylation. In HF, the distribution of mono-, di-, tris-, and tetra-phosphorylated cMyBP-C shifts from tris- and tetra-phosphorylated molecules (constituting ~65%) in healthy hearts to predominantly unphosphorylated and mono-phosphorylated cMyBP-C molecules (constituting ~88% in total) [29,31–33]. Mice expressing phosphomimetic charge substitutions at cMyBP-C phosphoserines display cardioprotective phenotypes, evident by preserved cardiac morphology [34], enhanced myocardial relaxation [18] and attenuated age-related cardiac dysfunction [35]. Moreover, in a rat HF model, reduced cMyBP-C phosphorylation coincided with decompensation [36], further supporting cMyBP-C phosphorylation as a target for new therapy in diseased myocardium. The present study focuses on the N-terminal region of cMyBP-C as this is the region responsible for the highly dynamic phosphoregulated interactions with actin and myosin that modulate cMyBP-C function.

Human cMyBP-C N-terminal fragment C0-C2 is ~50 kDa and contains two flexible linker regions, the proline/alanine-rich linker (P/A) connecting C0 to C1 and the motif domain (M-domain) (Fig. 1C). The M-domain is largely intrinsically disordered and contains four serines phosphorylated by PKA at positions 275, 284, 304, and 311 [5,37]. The C-terminal portion of the M-domain contains a structured three helix bundle at residues 322–357 termed the tri-helix bundle [38]. In the present work, we built on the previous findings in mouse C0-C2 [39] to identify labeling sites in human C0-C2 that are responsive to PKA-mediated phosphorylation as detected by TR-FRET. Using site-directed mutagenesis, cysteine pairs (di-Cys) were introduced for donor and acceptor probe labeling to examine four different regions in C0-C2 between C1 and the M-domain (Fig. 1C-E).

In the present study, we examine cMyBP-C C1-M-domain dynamics regulated by phosphorylation to better understand structural perturbations associated with physiological cMyBP-C function. We describe the identification and characterization of C0-$C2^{Cys225.Cys330}$, a di-Cys C0-C2 biosensor that is sensitive to PKA-catalyzed phosphorylation. C0-$C2^{Cys225.Cys330}$ labeled with the fluorescent dye (5-((((2-Iodoacetyl) amino)ethyl)amino)Naphthalene-1-Sulfonic acid (IAEDANS) and a FRET acceptor N-(4-(dimethylamino)-3,5-dinitrophenyl)maleimide (DDPM) reports changes in FRET efficiency upon phosphorylation. These changes indicate that the distance and molecular disorder between these probes is increased. Validation studies showed C0-$C2^{Cys225.Cys330}$ retains wild type C0-C2 secondary structure, levels of phosphorylation, and actin-binding function. Using a fluorescence lifetime plate reader (FLTPR) and detection of phosphorylation-mediated changes in biosensor lifetimes, C0-$C2^{Cys225.Cys330}$ offer the unique capability to screen thousands of compounds for their ability to bind to C0-C2 and mimic the changes brought about by phosphorylation. By applying a *Z'*-factor statistical test, we demonstrate that our biosensor is an excellent tool for use in high-throughput screening (HTS) to identify small-molecule compounds that bind cMyBP-C and modify its structure to mimic phosphorylated N-terminal structural dynamics. To further validate the biosensor and gain new mechanistic insights, we used the biosensor to evaluate TR-FRET effects of mutating the PKA sites from serine to aspartic acid to mimic the negative charge of phosphorylation and determined effects of the HCM-causing mutation R282W [40]. While the primary goal of this work was to develop a compound

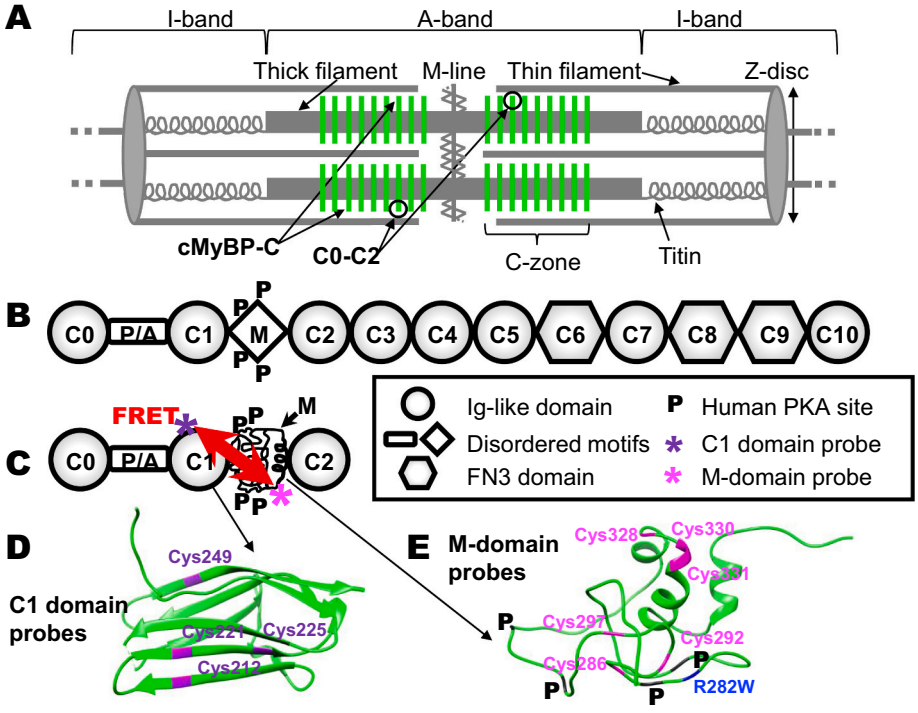

Fig. 1. Sarcomere localization, domain organization, and di-Cys biosensors of cMyBP-C. *(A)* The sarcomere spans from Z-disc to Z-disc with the A-band containing thick filaments and the I-band containing actin filaments. Force is generated by myosin and actin in the thin/thick filament overlap portion of the A-band. cMyBP-C molecules (green vertical stripes) are present in the C-zones towards the center of the A-band. Titin molecules anchor in the Z-disc and extend to the M-line. *(B)* Full-length cMyBP-C domains C0 through C10. Ig-like domains are shown as circles and fibronectin type-III domains (FN3) are shown as hexagons. *(C)* N-terminal domains C0 through C2 (C0-C2), containing the proline/alanine-rich linker (P/A) and the M-domain (M) that contains phosphorylation sites (P). *(D)* C1 domain structure (green, PDB: 2V6H) illustrating sites of probe-conjugated cysteines (Cys) tested (purple) listed numerically by primary amino acid sequence. *(E)* M-domain structure (green, from [39], based on PDB: 2LHU) with sites of probe-conjugated Cys tested (pink), PKA-mediated phosphorylation sites (black P's), and R282W HCM mutation (blue).

screening platform, TR-FRET data from the selected di-Cys C0-C2 biosensor adds mechanistic details into the structural dynamics of N-terminal cMyBP-C.

2. Materials and methods

2.1. Recombinant human cMyBP-C

A pET45b vector encoding *E. coli* optimized codons for the C0-C2 fragment of human cMyBP-C with N-terminal 6× His tag and TEV protease cleavage site was obtained from GenScript (Piscataway, NJ). C0-C2 biosensor mutants were engineered using a Q5 Site-Directed Mutagenesis Kit (New England Bio Labs, Ipswich, MA). Substitution mutations were performed to remove endogenous cysteines to generate C0-$C2^{C249S}$, C0-$C2^{Cys249}$, and C0-$C2^{Cys\text{-}free}$ constructs. C0-$C2^{Cys249}$ was generated by performing the following mutations: C239L, C426T, C436V, and C443S. C0-$C2^{Cys\text{-}free}$ was generated by performing the mutations: C239L, C249S, C426T, C436V, and C443S. Using the C0-$C2^{Cys249}$ template, the following mutations were introduced to generate di-Cys C0-C2 biosensors: S286C, I292C, S297C, A328C, P330C, or S331C. These are referred to as C0-$C2^{Cys249.Cys286}$, C0-$C2^{Cys249.Cys292}$, C0-$C2^{Cys249.Cys297}$, C0-$C2^{Cys249.Cys328}$, C0-$C2^{Cys249.Cys330}$, and C0-$C2^{Cys249.Cys331}$, respectively. Using the C0-$C2^{Cys\text{-}free}$ template, mutations were introduced to generate mono-Cys C0-C2: S212C, L221C, or H225C. These are referred to as C0-$C2^{Cys212}$, C0-$C2^{Cys221}$, and C0-$C2^{Cys225}$, respectively. An additional cysteine was substituted into the mono-Cys C0-C2 to generate di-Cys C0-C2 biosensors (S297C and P330C) referred to as C0-$C2^{Cys212.Cys297}$, C0-$C2^{Cys212.Cys330}$, C0-$C2^{Cys221.Cys330}$, C0-$C2^{Cys225.Cys297}$, and C0-$C2^{Cys225.Cys330}$. On the selected biosensor background construct, C0-$C2^{Cys225.Cys330}$, 4 additional mutations were made (S275D, S284D, S304D, and S311D) to generate C0-C2-4SD$^{Cys225.Cys330}$ or 1 additional mutation, R282W, was made to generate C0-C2-R282W$^{Cys225.Cys330}$. All sequences were confirmed by DNA sequencing (Eton Biosciences, San Diego, CA).

Protein production in *E. coli* BL21(DE3) competent cells (New England Bio Labs, Ipswich, MA) and purification of C0-C2 proteins using His60 Ni Superflow resin was done as previously described [41]. The His-tag was removed by TEV protease digestion and C0-C2 was concentrated, dialyzed in 50/50 buffer (50 mM NaCl and 50 mM Tris, pH 6.5 or 7.5) and stored at 4 °C. Initial screening of C0-C2 biosensors was performed in 50/50 buffer at pH 7.5. C0-$C2^{Cys225.Cys330}$ constructs (wild type, 4SD, and R282W C0-$C2^{Cys225.Cys330}$ versions) were additionally purified using size exclusion chromatography to achieve >90% intact C0-C2. For size exclusion chromatography C0-C2 (10–15 mg/ml in 3.5–4.5 ml) was applied in running buffer (150 mM NaCl, 50 mM $NaPO_4$, 1 mM DTT, pH 6.7) to a HiPrep Sephacryl S-100 column. Flow rate was 0.7 ml/min. Purified C0-C2 was checked for purity by SDS-PAGE and then dialyzed into the appropriate buffer, usually 50/50 for labeling. At least two protein preparations were performed for each experiment and proteins were typically used within two weeks of purification.

2.2. Labeling of human C0-C2

C0-C2 labeling reactions were performed in 50/50 buffer in dim-lighting conditions. For donor and acceptor labeling, 60 μM of IAEDANS and 200 μM of DDPM was added to 50/50 buffer at pH 6.5 containing 50 μM C0-C2. For initial biosensor screening studies, C0-C2 was labeled at pH 7.5. For labeling, 50 μM C0-C2 was reduced using 0.2 mM tris(2-carboxyethyl)phosphine (TCEP) for 30 min at 25 °C while rocking. Dye stocks were thawed (stored at −80 °C in DMF) and added to C0-C2 while slowly vortexing. C0-C2 was labeled for 1 h at 25 °C, while rocking. After labeling, dithiothreitol (DTT) was added in 5× molar excess of dye concentration to terminate the reaction of unbound dye. Labeled C0-C2 was dialyzed against 50/50 buffer at 100× volume excess with two buffer changes to remove remaining dye and DTT. To remove any precipitated dye and insoluble C0-C2, donor-acceptor labeled C0-C2 was centrifuged for 30 min at 100,000 RPM (350,000 *xg*) in a Beckman TLA-120.2 rotor. The extent of protein labeling was determined by measuring dye absorbance at its maximal excitation wavelength using UV–Vis spectroscopy and dividing by the dye's extinction coefficient. Protein concentration was determined by Pierce™ BCA Protein Assay Kit (Thermo Fisher Scientific, Waltham, MA) as recommended by the supplier. Percent labeling was calculated by dividing the molar concentration of dye by the molar concentration of C0-C2 cysteines (50 μM of C0-C2 containing two cysteines is 100 μM of cysteines).

2.3. In vitro phosphorylation of cMyBP-C

For quantifying PKA-mediated phosphorylation of cMyBP-C, Pro-Q Diamond phosphoprotein stain was used to visualize phosphorylated C0-C2 and SYPRO Ruby stain was used for determining total protein according to the supplier's instructions (ThermoFisher, Waltham, MA). C0-C2 was dialyzed into either 50/50 buffer with 0.2 mM ATP, 1 mM DTT, and 2 mM $MgCl_2$ or MOPS-actin binding buffer (M-ABB; 100 mM KCl, 10 mM MOPS pH 6.8, 2 mM $MgCl_2$, 0.2 mM $CaCl_2$, 0.2 mM ATP, 1 mM DTT, and 1 mM sodium azide). C0-C2 was treated with 7.5 ng PKA/μg C0-C2 for 30 min at 30 °C. We previously determined that maximal phosphorylation is achieved at 2.5 ng PKA/μg C0C2 [42]. For quantifying sub-maximal phosphorylation levels, C0-C2 was treated with 0.125, 0.25, and 0.5 ng PKA/μg C0-C2 for 30 min at 30 °C [25].

2.4. Actin preparations

Actin was prepared from rabbit skeletal muscle by extracting acetone powder in cold H_2O as described [42]. The day prior to actin binding experiments (cosedimentation), G-actin was polymerized by the addition of $MgCl_2$ to a final concentration of 3 mM for 1 h at 25 °C. F-actin was collected by centrifugation at 4 °C, 100,000 RPM (350,000 *xg*) in a Beckman TLA-120.2 rotor and the pellet was resuspended in M-ABB. Any bundled actin was removed by centrifugation at 5000 *xg*, 4 °C for 5 min in an Eppendorf 5424R table-top microfuge.

2.5. Actin cosedimentation assays and binding analysis

Actin binding by cMyBP-C C0-C2 fragments was determined by cosedimentation and analyzed as previously described in detail [41]. Actin binding levels were determined at 25 °C in M-ABB using 1 μM phalloidin-stabilized F-actin incubated with 1.25 or 2.5 μM C0-C2 for 30 min.

2.6. Circular dichroism

Circular dichroism (CD) spectroscopy of wild type and donor-acceptor labeled C0-$C2^{Cys225.Cys330}$ constructs was performed to measure secondary structural content of C0-C2. CD spectra of 0.2 mg/ml of C0-C2 with a 0.5 mm pathlength cuvette were acquired on a DSM-20 CD spectrometer (Olis, Bogart, GA) in 20 mM sodium borate buffer (pH 7.0) with 1 mM DTT added one hour prior to readings at 25 ± 1 °C. Background signal was corrected by subtracting the spectra of the buffer from the C0-C2 spectra. 3 repeated scans of spectral readings were acquired at 1-nm intervals from 195 to 250 nm. Ellipticity from wavelengths 210 to 240 nm (by 1-nm increments) were analyzed for secondary structure analysis using predictive algorithms of the K2D3 web-based software [43].

2.7. Time-Resolved FRET (TR-FRET) data acquisition and analysis

50-μl sample aliquots were loaded in 384-well black polypropylene microplates (#781209, Greiner Bio-One, Monroe, NC). Plates were spun for 1 min at 1000 RPM (~200 *xg*) in an Eppendorf centrifuge and rotor (5810R A-4-81) to remove air bubbles. Donor (IAEDANS)-labeled or

donor-acceptor (IAEDANS-DDPM)-labeled C0-C2 (5 μM) was excited using a passively Q-switched microchip frequency-tripled Nd:YAG 355/532 nm combo laser (SNV-05P-100; Teem Photonics, Meylan, France) at 355 nm using a band-pass excitation filter (340/26 nm; Semrock, Rochester, NY) with a pulse repetition frequency of ~8 kHz. Emitted photons were passed through a polarizer set at the magic angle 54.7°, followed by an interference band-pass filter (470/20 nm; Semrock, Rochester, NY), and detected with a photomultiplier tube module (H10720–210; Hamamatsu Photonics, Hamamatsu, Japan) and 1 GHz analog transient waveform digitizer (ATWD version 3.1) (Kleinfelder, Proc. SPIE 2003) in a FLTPR instrument from Fluorescence Innovations (Minneapolis, MN). Fluorescence emission decays were acquired at 25 °C in 50/50 buffer with 0.2 mM ATP, 1 mM DTT, and 2 mM $MgCl_2$.

Fluorescence waveforms observed for each well of donor-only or donor-acceptor C0-C2 with or without PKA treatment were convolved with the instrument response function (IRF) to determine the lifetime (τ) (Eq. (1)). Data to analyze lifetimes to calculate FRET efficiency were fit to one-exponential decays using MatLab, version 7.1; The MathWorks. Fluorescence waveforms for donor-only (D_{only}) and donor-acceptor (D-A) labeled C0-$C2^{Cys225.Cys330}$ were analyzed using TR-FRET analysis software [44]. D_{only} waveforms were best-fit to three exponentials and D-A waveforms were best-fit to a one-Gaussian distance distribution determined by minimization of χ^2 values from the residual plots of the waveform fittings. The TR-FRET distance distribution was characterized by a center distance R_j between probes and a full width at half-maximum Γ_j (FWHM). See *Supplemental Methods* for additional details.

The decay of the excited state of the fluorescent IAEDANS donor dye attached to C0-C2 to the ground state is listed below in Eq. (1):

$$I(t) = I_0 exp\left(-\frac{t}{\tau}\right) \quad (1)$$

where I_0 is the peak fluorescence intensity upon excitation ($t = 0$) and τ is the fluorescence lifetime ($t = \tau$ when I decays to 1/e or ~37% of I_0). FRET efficiency values were calculated by Eq. (2) listed below:

$$\text{FRET Efficiency } (\%) = \left(1 - \frac{\tau_{DA}}{\tau_D}\right) \times 100 \quad (2)$$

where the τ_D and τ_{DA} represent lifetimes of D_{only} and D-A labeled C0-C2 biosensor, respectively. Percent change is calculated in Eq. (3) listed below as a function of FRET efficiency (E) biosensor with and without PKA treatment:

$$\%\text{Change} = \left(\frac{E_{+PKA} - E_{-PKA}}{E_{-PKA}}\right) \times 100 \quad (3)$$

2.8. Determination of Z′-factor for C0-$C2^{Cys225.Cys330}$

For suitability in high-throughput screening (HTS), TR-FRET assay quality was determined for unphosphorylated versus phosphorylated donor-acceptor labeled C0-$C2^{Cys225.Cys330}$. The lifetimes of unphosphorylated donor-acceptor labeled C0-$C2^{Cys225.Cys330}$ (τ_A) and phosphorylated donor-acceptor labeled C0-$C2^{Cys225.Cys330}$ (τ_B) were compared and indexed by the Z'-factor:

$$Z' = 1 - \frac{3(\sigma_A + \sigma_B)}{|\mu_A - \mu_B|} \quad (4)$$

where σ_A and σ_B are the standard deviations (S·D.) of the τ_A and τ_B lifetimes, respectively, and μ_A and μ_B are the means of the τ_A and τ_B lifetimes, respectively. Z'-factor of less than 0 is "useless", 0 to 0.5 is "good" and 0.5 to 1.0 is "excellent" assay quality [45].

2.9. Statistics

Average data are provided as mean ± standard error (S.E.) or standard deviation (S.D.), as indicated, and each experiment was done with >2 separate protein preparations. The level of significance (at least $p < 0.05$) for each Student's t-test and 1- and 2-way ANOVA using Tukey's posthoc was performed in GraphPad Prism version 9.0. Technical repeats (n, independent phosphorylation reactions) and biological repeats (independent protein preparations) are indicated in each figure and table.

3. Results

3.1. Modification of human C0-C2 for use in site-specific spectroscopy studies

To monitor structural dynamics in human cMyBP-C N-terminal regions (C0-C2, Fig. 1C), we attached FRET probes to different regions of the C1 and M-domains (Fig. 1D-E). Previous studies found that mouse C0-C2 is labeled with thiol-reactive FRET dyes only at one exposed cysteine, Cys248. The remaining four cysteines are buried in C1 and C2 and are not readily labeled [39,46]. Initial labeling tests of human protein resulted in dye:C0-C2 ratios that were much greater than 1:1 (as high as 4:1 for some probes, data not shown). For DDPM, labeling of wild type C0-C2 was 150% and DDPM labeling of C0-$C2^{C249S}$ that lacked the one surface exposed cysteine labeling was 40% (Fig. S1). This suggested that some of the 4 cysteines thought to be buried in human C1 and C2 were reactive during labeling in addition to Cys249 (the human residue homologous to mouse Cys248). Thus, for developing a biosensor, we substituted the 4 other cysteines by site-directed mutagenesis, leaving only the surface exposed Cys249 (referred to as C0-$C2^{Cys249}$) for labeling and introduction of a second cysteine for TR-FRET. To probe other regions of C1 besides Cys249, we removed all 5 endogenous cysteines (referred to as C0-$C2^{Cys\text{-}free}$) to allow for introduction of di-Cys pairs for FRET labeling. To avoid disruption of C1 and C2 domains, cysteines were replaced, when possible, with amino acids found in the homologous positions in other MyBP-C isoforms or species (Fig. S2).

3.2. Designing and testing of di-Cys C0-C2 FRET biosensors for detecting phosphorylation-dependent structural changes

TR-FRET between probes on C1 and C2 in mouse C0-C2 showed structural changes upon PKA phosphorylation [39]. Introduction of cysteines at multiple sites in C2 of human C0-$C2^{Cys249}$ resulted in destabilized and degraded protein being produced in bacteria (data not shown). Therefore, we used C0- $C2^{Cys249}$ and C0-$C2^{Cys\text{-}free}$ as templates to substitute additional cysteine(s) in the C1 and M-domains. Each potential FRET-based biosensor construct is a di-Cys C0-C2 protein designed to examine phosphorylation-sensitive structural dynamics between C1 and the M-domain (Fig. 1C-E). Placement of cysteine substitutions was designed to avoid phosphorylation sites, PKA recognition motifs, and highly conserved residues (Fig. S2).

.

The percent change in FRET efficiency that resulted from PKA treatment of 11 di-Cys constructs is shown in Table 1. Six constructs were tested using Cys249 in C1 paired with a second cysteine at positions within the phosphoserine region (positions 286, 292, or 297) or the tri-helix bundle region (positions 328, 330, or 331) of the M-domain. C0-$C2^{Cys249.Cys297}$ was the only construct tested with a PKA-mediated increase in FRET efficiency of ~2.9%, while C0-$C2^{Cys249.Cys330}$ reported the largest reduction of ~5.4%. Next, we surveyed structural changes with C1 probes placed on the other side of the Ig-like domain relative to Cys249. For this we generated C0-$C2^{Cys212}$, C0-$C2^{Cys221}$, and C0-$C2^{Cys225}$ constructs (Fig. 1D). These were paired with M-domain cysteines at either Cys297 or Cys330, as these locations reported the largest changes in C0-$C2^{Cys249}$ constructs. C0-$C2^{Cys225.Cys330}$ exhibited the largest PKA-mediated effect in FRET efficiency (further described in Figs. 2 and 3) and was selected for further characterization. Fluorescence waveforms of IAEDANS labeled C0-$C2^{Cys225.Cys330}$ (D_{only}) and IAEDANS plus DDPM

Table 1
Potential human C0-C2 biosensors: PKA-mediated phosphorylation effects on FRET efficiency.

Cysteine Location (C1 Domain.M-domain)	Percent change in FRET Efficiency	Number of PKA Treatments	Number of Protein Preparations
Cys249.Cys286	−0.8 ± 0.1	5	2
Cys249.Cys292	−2.3 ± 1	9	4
Cys249.Cys297	2.9 ± 0.4	4	2
Cys249.Cys328	−1.3 ± 0.5	7	3
Cys249.Cys330	−5.4 ± 0.6	7	3
Cys249.Cys331	−3.4 ± 0.5	7	3
Cys212.Cys297	−7.8 ± 1.5	5	2
Cys225.Cys297	−5.1 ± 0.9	6	2
Cys212.Cys330	−11.8 ± 0.6	5	2
Cys221.Cys330	−17.2 ± 0.7	10	3
Cys225.Cys330	−18.2 ± 0.6	6	2

Primary sequence location of cysteines in C1 and M-domain of each human di-Cys C0-C2 biosensor tested. FRET efficiency was calculated using Eq. 2 from donor and donor-acceptor lifetimes for each biosensor ±phosphorylation. Percent change in FRET efficiency due to phosphorylation is calculated using Eq. 3 and shown as mean ± S.E., n = 4-10 (2 preparations). The number of replicates for individual phosphorylation treatments (technical repeats) and protein preparations (biological repeats) are shown in columns on the right side.

labeled C0-C2$^{Cys225.Cys330}$ (D-A) are shown in Fig. 2A. The presence of the acceptor (D-A) causes a leftward shift of the waveform (relative to D_{only}) due to FRET. The effect of phosphorylation is observable on the D-A waveform causing a rightward shift indicating less FRET (Fig. 2B-C). Fluorescence lifetime of D_{only} and D-A samples derived from waveforms are shown in Fig. 3 and FRET efficiencies were calculated from these lifetimes. FRET reduced lifetime in D-A samples (11.47 ± 0.04 ns) compared to D_{only} samples (14.42 ± 0.04 ns) (Fig. 3A). PKA treatment of D-A C0-C2 increases lifetime by 3.4% (Fig. 3A-B) and significantly reduces FRET efficiency from 20.4 ± 0.2% to 16.8 ± 0.2% ($p < 0.0001$) (Fig. 3C), indicating a 17.5 ± 0.4% reduction in FRET Efficiency (Table 1). Interestingly, a small (1.1%) but significant reduction in lifetime of IAEDANS upon PKA treatment is observed for D_{only} C0-C2$^{Cys225.Cys330}$ (14.24 ± 0.04 ns), suggesting small but detectable effects of phosphorylation on the probe environment.

3.3. *Evaluation of cMyBP-C biosensor C0-C2$^{Cys225.Cys330}$ suitability for high-throughput screening (HTS)*

We tested C0-C2$^{Cys225.Cys330}$'s suitability as a sensor in mock screens for small-molecule drugs that bind to unphosphorylated C0-C2 and induce N-terminal structural (e.g., changes that recapitulate phosphorylated structural dynamics) by determining a *Z'*-factor. Lifetime averages and standard deviations (S.D.) of the donor probe (IAEDANS) in donor-acceptor (IAEDANS-DDPM) labeled C0-C2$^{Cys225.Cys330}$ were determined for non-phosphorylated and phosphorylated C0-C2$^{Cys225.Cys330}$. These values were then used to calculate *Z'*-factor (Eq. (4)). *Z'*-factors less than 0 indicate that screens done under the conditions tested would be useless. *Z'*-factors between 0.0 and 0.5 indicate a doable screen

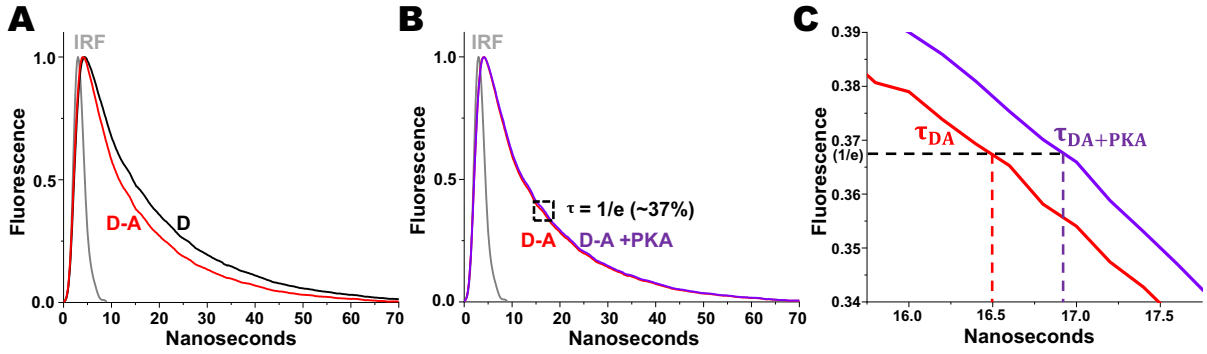

Fig. 2. Fluorescence lifetime decays for TR-FRET of C0-C2 biosensor. *(A)* Normalized TR-FRET waveform decays of 5 μM C0-C2$^{Cys225.Cys330}$ biosensor. Instrument response function (IRF) of water scattering is shown in grey. Donor-only (D, black) and donor-acceptor (D-A, red) samples exhibit waveform decays after the initial rising phase due to IAEDANS excitation. *(B)* Waveform decays of D-A labeled unphosphorylated C0-C2$^{Cys225.Cys330}$ (red) and PKA-phosphorylated C0-C2$^{Cys225.Cys330}$ (purple). Region of fluorescence lifetime, where τ decays to 1/e (~37%) of the peak intensity, is highlighted by dotted box. *(C)* Magnified dotted box region in panel *B*. Actual lifetime is ~5 ns less than shown on x-axis due to rising phase of excitation from 0 to ~5 ns (e.g., τ_{DA} is ~11.5 instead of 16.5 ns).

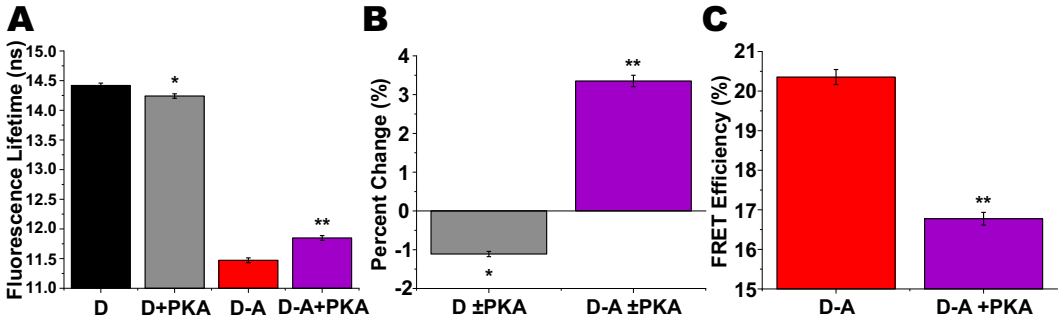

Fig. 3. PKA-mediated phosphorylation effects on C0-C2 biosensor. *(A)* Donor-only (D) and donor-acceptor (D-A) without or with PKA phosphorylation (+PKA) lifetimes of C0-C2$^{Cys225.Cys330}$ biosensor derived from waveforms like those in Fig. 2. *(B)* Percent change (%) in lifetimes of D and D-A samples upon PKA treatment. *(C)* FRET Efficiency (%) of D-A samples without and with PKA-mediated phosphorylation of C0-C2 biosensor. Data shown as mean ± S.E., $n = 35–38$ (9 preparations). For each panel comparing with and without PKA, $^{*}p < 0.002$, $^{**}p < 0.0001$ (Student's *t*-test).

and *Z'*-factors between 0.5 and 1.0 are indicative of an excellent screen [45]. Using a 384-well plate, D-A C0-C2$^{Cys225.Cys330}$ was tested for PKA-mediated changes in lifetime. Fig. 4 shows 76 wells of D-A biosensor plotted as a function of IAEDANS lifetime. The average lifetimes of unphosphorylated and phosphorylated C0-C2$^{Cys225.Cys330}$ are 11.50 ± 0.03 ns and 11.85 ± 0.02 ns, respectively (Fig. 4). This difference of 3.04% is highly significant ($p < 0.0001$). The *Z'*-factor for this comparison is 0.60, which classifies our assay as "excellent" for use in HTS. Furthermore, this was repeated with 9 independent protein preparations and in each case *Z'*-factors were confirmed to be in the excellent range (Table 2).

3.4. Evaluating the effects of PKA-mediated phosphorylation on C0-C2$^{Cys225.Cys330}$ structural dynamics

TR-FRET waveforms were analyzed globally for C0-C2$^{Cys225.Cys330}$ to determine the effect of phosphorylation on the center distance (R_j,) and the distribution of distances, expressed as FWHM (Γ_j), between the probes as an indicator of molecular disorder. C0-C2 phosphorylation causes an increased distance and wider distribution of the structural population as indicated by increases in R_j and Γ_j. Fig. 5A shows phosphorylation significantly increases R_j by 10.5% from 32.83 ± 0.65 Å to 36.27 ± 0.60 Å ($p < 0.002$), a ΔR_j of 3.44 Å. Fig. 5B shows phosphorylation significantly increases Γ_j by 30.4% from 21.65 ± 0.41 Å to 28.24 ± 0.40 Å ($p < 0.0001$), a $\Delta\ \Gamma_j$ of 6.59 Å. Both unphosphorylated and phosphorylated IAEDANS-DDPM labeled C0-C2$^{Cys225.Cys330}$ were best-fit to a one-Gaussian distance distribution and shown in Fig. 5C. Fig. 5D shows a C0-C2 cartoon illustrating these changes to C0-C2 structure.

3.5. C0-C2$^{Cys225.Cys330}$ retains wild type secondary structure

CD spectroscopy was used to quantify the secondary structural content (α-helix, β-sheet, and turns/undefined) of wild type C0-C2 and labeled C0-C2$^{Cys225.Cys330}$. The molar residue ellipticity values plotted against wavelength were similar for both C0-C2 constructs (Fig. 6A). Each displayed a single, broad negative band in the far-UV wavelength region (200–220 nm) permitting well-defined calculation of secondary structure content. For wild type and biosensor C0-C2, α-helical content was estimated to be, 2.3% and 2.8%, β-sheet content was estimated to be 38.6% and 38.5%, and turns/undefined to be 59.1% and 58.8%, respectively.

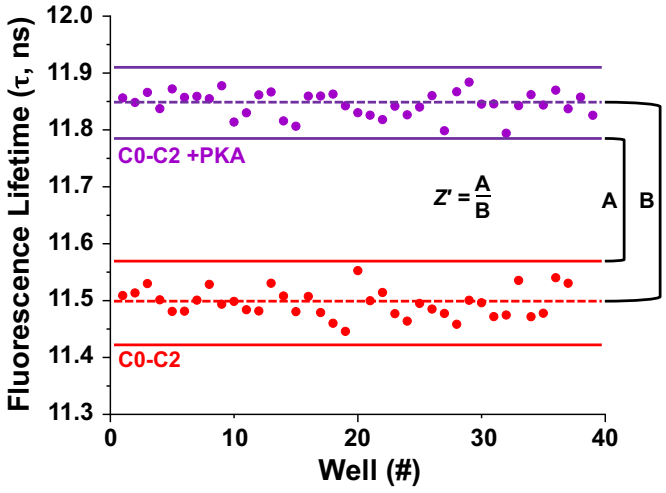

Fig. 4. *Z'*-factor test comparing unphosphorylated and phosphorylated C0-C2 biosensor lifetimes. Lifetimes of 5 μM D-A labeled C0-C2 biosensor without (red) or with PKA treatment (purple) in ~40 wells each of a 384-well plate. In this test, each +PKA well was treated independently with PKA. Horizontal solid lines indicate 3× S.D. of the mean lifetimes (dotted line). *Z'*-factor is defined as the difference between 3× S.D. (A) divided by the difference in the mean signal (B) (Eq. (4)). In this test the *Z'*-factor is 0.60.

3.6. C0-C2$^{Cys225.Cys330}$ exhibits normal sensitivity to PKA-mediated phosphorylation

PKA-mediated phosphorylation of wild type C0-C2 and C0-C2$^{Cys225.Cys330}$ was compared using Pro-Q Diamond phospho-staining and SYPRO Ruby total protein staining. Using our standard conditions, no difference was found at maximal phosphorylation levels (Fig. 6B), indicating that phosphorylation is normal in the biosensor. Testing phosphorylation over a range of PKA concentrations previously shown to cause sub-maximal phosphorylation [25] showed that C0-C2 and C0-C2$^{Cys225.Cys330}$ were equally phosphorylated at each concentration (Fig. S3).

3.7. C0-C2$^{Cys225.Cys330}$ maintains cMyBP-C C0-C2 actin-binding function

We evaluated C0-C2$^{Cys225.Cys330}$ and wild type C0-C2 actin binding by using a filamentous actin (F-actin) cosedimentation assay. We and others have found that wild type C0-C2 binding increases in a concentration-dependent manner and is significantly reduced by PKA phosphorylation [25,27]. The most useful comparisons are found at submaximal binding levels (MyBP-C:actin; 1:7) [25], consistent with the ratios found in cardiac muscle. C0-C2$^{Cys225.Cys330}$ binding to actin was concentration- and PKA phosphorylation-dependent and similar to that observed for wild type C0-C2 (Fig. 6C).

3.8. Phosphomimetic substitutions of the 4 PKA sites in C0-C2$^{Cys225.Cys330}$ recapitulate changes in structural dynamics due to kinase treatment

As a proxy for the negative charge associated with phosphorylation, we substituted each PKA-mediated phosphoserine with an aspartic acid (S275D, S284D, S307D, and S311D) in the C0-C2$^{Cys225.Cys330}$ biosensor, termed C0-C2-4SD$^{Cys225.Cys330}$. Fig. 7A shows the effect of the 4SD mutation on the C1-M-domain spatial positioning relative to the wild type biosensor in the presence and absence of phosphorylation. The distance distribution of unphosphorylated 4SD shows an increase in the center distance (R_j) by 16% ($p < 0.004$) and broadening in the width of the distribution (FWHM, Γ_j) by 33% ($p < 0.0001$) relative to unphosphorylated C0-C2$^{Cys225.Cys330}$. Further, unphosphorylated 4SD was not different from phosphorylated wild type biosensor (R_j: $p = 0.19$ and Γ_j: $p = 0.34$). As expected, PKA treatment had no effect on C0-C2-4SD$^{Cys225.Cys330}$ (R_j = 37.93 ± 1.19 Å versus 37.57 ± 0.88 Å, $p = 0.82$ and Γ_j = 28.87 ± 0.03 Å versus 29.23 ± 0.47 Å, $p = 0.49$, respectively). Interestingly, Fig. S6 shows that 4SD effects on biosensor FRET efficiencies were intermediate between unphosphorylated and phosphorylated wild type (see *Supplemental Results*).

3.9. Effects of HCM mutation R282W on C0-C2$^{Cys225.Cys330}$ FRET efficiency and level of phosphorylation

To ask if the C0-C2$^{Cys225.Cys330}$ biosensor is able to detect structural changes due to an HCM mutation, R282W, known to reduce MyBP-C phosphorylation by PKA, we introduced this mutation into the biosensor, C0-C2-R282W$^{Cys225.Cys330}$. This mutation modifies the PKA-recognition motif preceding Ser284 from R-R-I-S^{284} to R-W-I-S^{284} [40]. Fig. 7B shows the effects of R282W on the C1-M-domain distance distributions in C0-C2$^{Cys225.Cys330}$ and changes due to PKA treatment. In unphosphorylated and phosphorylated states, the distances between probes are reduced in R282W compared to C0-C2$^{Cys225.Cys330}$. Specifically, unphosphorylated R282W R_j is 29.95 ± 0.15 Å and Γ_j is 20.00 ± 0.12 Å and in the phosphorylated state, R282W R_j is 31.81 ± 0.13 Å and Γ_j is 21.13 ± 0.10 Å. In each condition, R282W R_j and Γ_j values are significantly reduced relative to C0-C2$^{Cys225.Cys330}$ ($p < 0.05$). In terms of percent change, R282W phosphorylation causes a 6.2% increase in R_j compared to 10.5% in C0-C2$^{Cys225.Cys330}$, and a 5.7% increase in Γ_j

Table 2
Z'-factor Score for D-A C0-C2$^{Cys225.Cys330}$ ± PKA.

(#) Preparation	Number of wells (n)	D-A Lifetime (ns)	D-A + PKA Lifetime (ns)	Lifetime Difference (ns)	Sum of 3×S.D.	*Z'*-factor
Prep. 1	28	11.71	12.00	0.29	0.10	0.67
Prep. 2	20	11.61	11.96	0.36	0.08	0.77
Prep. 3	18	11.64	11.95	0.31	0.09	0.70
Prep. 4	20	11.17	11.58	0.40	0.09	0.78
Prep. 5	32	11.42	11.87	0.45	0.09	0.79
Prep. 6	22	11.37	11.86	0.49	0.12	0.75
Prep. 7	10	11.27	11.54	0.28	0.11	0.61
Prep. 8	10	11.38	11.76	0.38	0.10	0.73
Prep. 9	76	11.50	11.85	0.35	0.14	0.60

Evaluating the Z'-factor for 9 protein preparations of donor-acceptor labeled C0-C2Cys225.Cys330. Mean lifetimes and lifetime differences (±phosphorylation) were calculated from multiple wells (n) of donor-acceptor labeled C0-C2Cys225.Cys330 from 9 independent protein preparations. The sum of 3standard deviations (3S.D.) from unphosphorylated and phosphorylated lifetimes for each test is shown (Sum of 3S.D). Z'-factors were calculated using Eq. 4. For Preparation 9, phosphorylation was done separately for each of 37 wells. For Preparations 1-8, phosphorylation was done in bulk batch and aliquoted into different wells. See Fig. 4 for an example (Preparation 9) of Z'-factor test data.

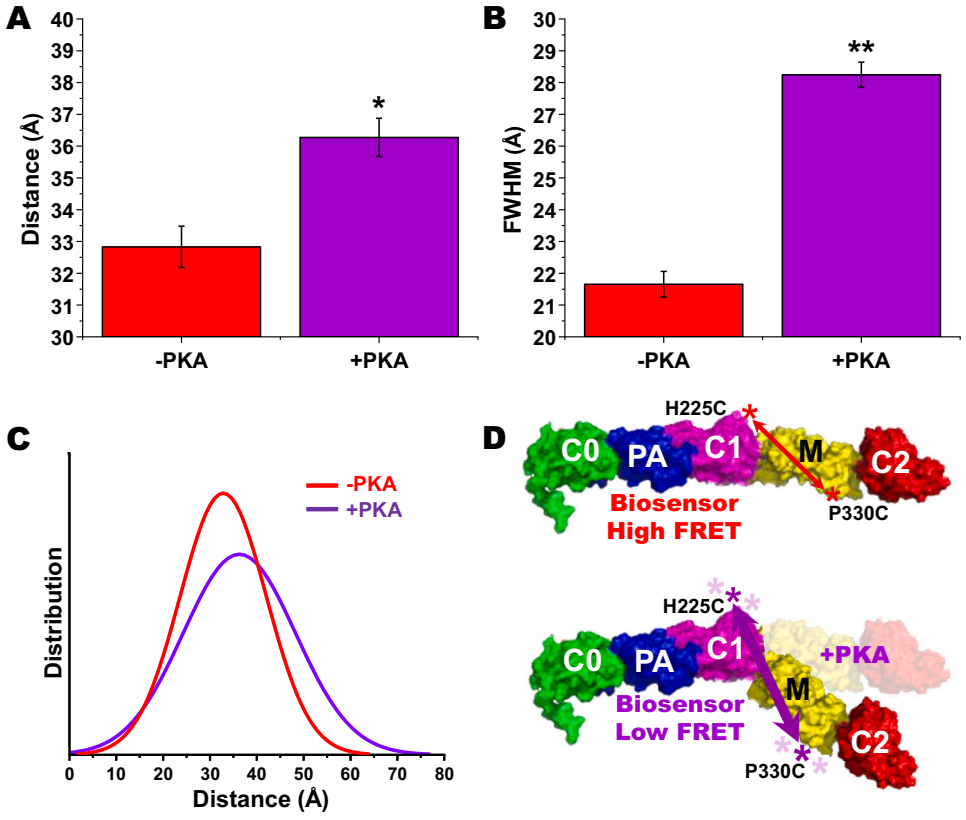

Fig. 5. Effects of PKA-mediated phosphorylation on structural dynamics of C0-C2 biosensor. Global analysis of TR-FRET waveforms used non-linear least squares regression. *(A)* Center distances of C0-C2 biosensor without (red) and with (purple) PKA treatment. *(B)* FWHM of C0-C2 biosensor without (red) and with (purple) PKA treatment. *(C)* Distance distribution plot generated from center distances and FWHM values of C0-C2 biosensor without (red) and with (purple) PKA treatment. *(D)* Cartoon of changes in structure that would be consistent with TR-FRET data showing distance (length of double-sided arrows) and dynamics (arrow thickness and faded protein structure with multiple *'s representing disorder) of C0-C2 biosensor. Overall changes in C0-C2 shape (bending and compactness with phosphorylation) are based on earlier findings by us and others [23,39]. Image modified from PDB model in [47]. For panels *A* and *B*, data shown as mean ± S.E., $n = 7$ (4 preparations), and $^{*}p < 0.002$ and $^{**}p < 0.0001$ (Student's *t*-test).

compared to 30.4% in C0-C2$^{Cys225.Cys330}$. Fig. S6 shows that R282W effects on biosensor FRET Efficiencies were different from wild type for both unphosphorylated and phosphorylated conditions (see *Supplemental Results*).

4. Discussion

In the present study, we have identified therapeutically and physiologically relevant conformational changes in the cMyBP-C molecule. We employed TR-FRET to measure changes in FRET efficiency and structural dynamics of phosphorylated and unphosphorylated states of cMyBP-C N-terminal domains C0-C2. The ability to monitor structural changes in C0-C2 using a recently developed FLTPR instrument makes possible the screening of large compound libraries for compounds that bind to human C0-C2 and mimic the effects of phosphorylation-mediated structural dynamics. We have recently used similar technology to screen for compounds that bind C0-C2 and interfere with its actin binding activity [48].

4.1. Lifetime measurement of D-A labeled C0-C2$^{Cys225.Cys330}$ is a biophysical assay suitable for use in HTS

Using a FLTPR, we are equipped to monitor changes in lifetime of fluorescent probes attached to proteins in a 384-well plate format. The instrument scans all wells in less than 3 min (~0.5 s/well), meaning that the instrumentation is available to screen large compound libraries for compounds that mimic changes in lifetime of a fluorescent probe brought about by physiologically relevant structural changes. For cMyBP-C, TR-FRET with donor and acceptor probe sites located in the C1 and M-domains demonstrates that we can monitor the change in structure that takes place upon PKA-mediated phosphorylation (Figs. 1-3, Table 1). To determine the quality of this assay for use in HTS, we

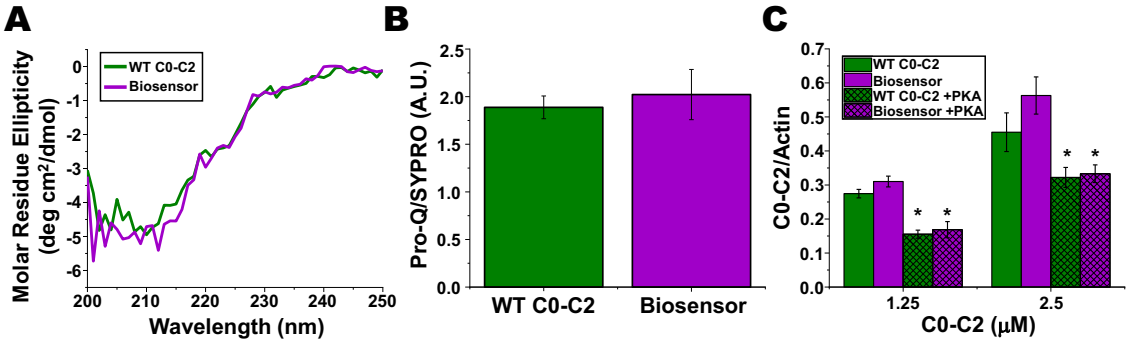

Fig. 6. C0-C2 biosensor retains wild type secondary structure, phosphorylation, and phosphorylation-sensitive actin binding. *(A)* CD spectroscopy shows the wavelength dependence of molar residue ellipticity (MRE) values of wild type (green) and C0-C2$^{Cys225.Cys330}$ biosensor (purple) were similar, indicating similar secondary structural content. *(B)* Maximal phosphorylation levels with 7.5 ng PKA/μg of wild type (green) and C0-C2$^{Cys225.Cys330}$ biosensor (purple) by using Pro-Q Diamond/SYPRO staining intensity ratios were not significantly different. *(C)* Actin cosedimentation assays for molar binding of unphosphorylated and phosphorylated wild type and C0-C2$^{Cys225.Cys330}$ biosensor were similar. For all proteins and concentrations tested, PKA reduced C0-C2 binding, indicating normal actin-binding function of the biosensor. Data shown as mean ± S.E., $n = 6–9$ (2 preparations). For panel *C*, * denote statistical differences due to PKA phosphorylation of WT and biosensor for each respective C0-C2 concentration, $*p < 0.0001$ (1-way ANOVA, Tukey's multiple comparisons).

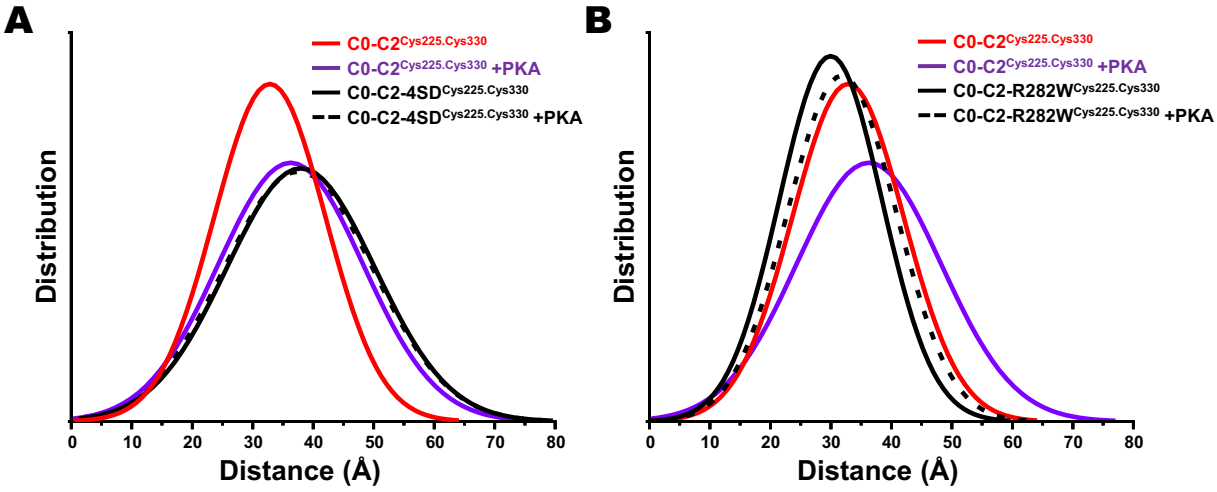

Fig. 7. Effects of phosphomimetic substitutions (4SD) and HCM mutation (R282W) on unphosphorylated and phosphorylated Cys225.Cys330 distance distributions. *(A-B)* Distance distributions of C0-C2 biosensor without (red) and with (purple) PKA treatment. Each population possesses a center distance (peak) and measure of disorder (FWHM) in angstroms (Å). *(A)* Distance distributions of C0-C2-4SD$^{Cys225.Cys330}$ without (solid black line) and with (dashed black line) PKA treatment. *(B)* Distance distributions of C0-C2-R282W$^{Cys225.Cys330}$ without (solid black line) and with (dashed black line) PKA treatment. Data shown as mean (distance and FWHM), $n = 3–7$ (>2 preparations per construct).

determined the *Z'*-factor by comparing unphosphorylated and phosphorylated (IAEDANS-DDPM (D-A)) labeled C0-C2$^{Cys225.Cys330}$ lifetimes (Fig. 4, Table 2) in a mock screen. With a *Z'*-factor of ~0.60, we developed an "excellent" assay that readily reports two distinct lifetime populations with a mean difference of 350 ps or 3%. Although the percent change in lifetime is small, at the biophysical scale with the FLTPR sensitivity and precision, a 3.04 ± 0.04% change is very significant ($p < 0.0001$) with each population (unphosphorylated and phosphorylated) exhibiting coefficient of variances (a measure of precision) of <0.25%, and standard errors (S.E.) of ≤0.004. This establishes the suitability of the cMyBP-C biosensor and structure-based assay for use in HTS. Therefore, our novel in vitro biophysical assay is positioned to aid in the discovery of small-molecule effectors that regulate cMyBP-C structure, and thereby advance drug discovery efforts to correct contractile dysfunction by targeting this critical sarcomeric protein.

4.2. C0-C2$^{Cys225.Cys330}$ retains native structure, phosphorylation, and actin binding activities

For making the C0-C2$^{Cys225.Cys330}$ biosensor, seven mutations were required to remove the five endogenous cysteines and add two new cysteines for labeling. It was therefore important to test for any modifications in the mutant C0-C2 structure and function. We assessed C0-C2$^{Cys225.Cys330}$ for changes in secondary structure, level of phosphorylation, and C0-C2 actin-binding function due to cysteine mutagenesis and D-A labeling (Fig. 6). CD spectra and application of the K2D3 algorithm estimated secondary structure (α-helical, β-sheet, and turns/undefined) and detected no differences (Fig. 6A). This suggests mutagenesis and labeling did not alter secondary structural content of the N-terminal IgI-like domains and flexible linkers. The extent of PKA-mediated phosphorylation of C0-C2$^{Cys225.Cys330}$, as reported by Pro-Q Diamond staining, was also similar to levels detected in wild type, further validating that those mutations and labeling did not affect the responsiveness of the M-domain to PKA-mediated phosphorylation at maximal (Fig. 6B) and sub-maximal (Fig. S3) levels. The function of C0-C2 was assessed by cosedimentation assays with F-actin (Fig. 6C). Molar binding ratios of C0-C2/actin and C0-C2$^{Cys225.Cys330}$/actin increased in a concentration-dependent manner and demonstrated significant reductions upon phosphorylation. In each experimental condition, molar binding ratios of C0-C2/actin were similar, further validating that

mutations did not perturb C0-C2 function. That there were no changes in structure or function was expected based on their design. For the replacement of existing cysteines, most (4 of 5 substitutions) were replaced with amino acids found at the homologous position in cMyBP-C of other species or in other isoforms of MyBP-C (Fig. S2). For the addition of cysteines to use for probe attachment, we selected amino acids whose side chains occurred on the surface of C1 or the tri-helix bundle in existing structures and did not disrupt the PKA recognition sequences (K/R,K/R,X,X,S) or sites in the M-domain (Fig. S2). Additionally, when possible, we selected to replace (with cysteines) amino acids that showed low sequence homology across species and MyBP-C isoforms (Fig. S2). Our recent work using single-cysteine C0-C2^{Cys225} labeled with an acceptor probe to follow binding to donor-labeled F-actin found saturable actin binding that was reduced upon phosphorylation [48]. Therefore, C0-C2$^{Cys225.Cys330}$ is a functional biosensor for HTS and uncovering mechanistic details of cMyBP-C molecular structure and the effects of phosphorylation in C1-M-domain dynamics.

4.3. Examining phosphorylation-induced changes in the N-terminal structural dynamics between C1 and the M-domains

Using TR-FRET, we can detect structural changes in cMyBP-C to gain insight into how phosphorylation regulates N-terminal structure. Recent findings by Rahmanseresht et al. [12] suggest that in relaxed muscle, cMyBP-C N-terminus is either unbound occupying the interfilament space between myosin and actin or bound to actin. Interestingly, in ~80–90% of the images, the N-terminus appeared to be unbound, implicating an increased physiological relevance of unbound N-terminal molecular changes reported here. Fig. 1D-E shows Cys255 is localized in the 6th β-sheet of C1 and Cys330 is localized in the C-terminal end of the first α-helix of the tri-helix bundle. The spatial positioning between Cys255 and Cys330 constitutes a dynamic, structural population best fit to a one-Gaussian distribution (Fig. 5A). Analyzing this population to determine the effects of phosphorylation revealed changes in the N-terminal structural dynamics. We report a modest yet significant 10.5% increase in distance, and a substantial 30.4% increase in the distance distribution (FWHM) upon PKA-mediated phosphorylation of C0-C2 (Fig. 5B-C). Thus, the 17.5% reduction in FRET efficiency with phosphorylation is due to changes in both distance and disorder between Cys225 and Cys330. Phosphorylation shifts the structural populations towards a more disordered state that is slightly further apart. Previous TR-FRET studies of mouse C0-C2 found phosphorylation *reduced* distance and disorder between C0 and C1 as well as between C1 and C2. This results in global changes of the N-terminal region, C0-C2, causing the molecule to be more compact [39]. Using rotary-shadowed electron microscopy of mouse C0-C3, Previs et al. [23] suggested the presence of a hinge point within the M-domain that dictates 3 conformational states (extended, bent, and compact) of the C0-C3 molecule. They showed that phosphomimetic substitutions in C0-C3 causes a ~4×-fold increase in the "compact" conformation and ~8×-fold reduction in the extended conformation [23]. These findings and our results showing that phosphorylation *increases* disorder and distance between sites in C1 and the tri-helix bundle in the M-domain emphasize the potential complexity in cMyBP-C's phosphoregulated molecular changes. Phosphorylation could decrease the distance between C1 and C2 by an overall more compact M-domain or a bending of the M-domain. The latter could result in increases in distances between points in C1 and the M-domain (Fig. 5D). Examination of additional labeling sites in the M-domain, C0, C1 and C2 are needed to resolve these details in human cMyBP-C but are beyond the scope of the current work.

4.4. Implications for mechanism of cMyBP-C phosphorylation in cardiac physiology

β-adrenergic signaling modifies cardiac myosin cross-bridge cycling kinetics by altering the phosphorylation state of thick and thin filament proteins, including cMyBP-C [19]. Changes in cMyBP-C phosphorylation levels are believed to modify force development by regulating N-terminal C0-C2 interactions with myosin and actin. Phosphorylation reduces binding to both and is associated with accelerated contractile kinetics. This suggests that cMyBP-C is a tunable regulator in myocardial contractility. Our previous work with mouse C0-C2 indicated that PKA-mediated phosphorylation regulates its structural dynamics, and that this regulation could be readily monitored by TR-FRET [39]. The present study provides additional insight into functionally relevant conformational changes in this cMyBP-C. One possibility is that altered structure and dynamics of C0-C2 leads to altered binding and/or structural dynamics of the bound complex with actin or myosin. The identification and development of a TR-FRET phosphorylation-sensitive biosensor (C0-C2$^{Cys225.Cys330}$), and the ability to introduce probes at other residues, provides a new research tool to resolve mechanistic details of human N-terminal cMyBP-C structural dynamics.

4.5. Role of negative charge in phosphomimetic biosensor and physiological implications

To examine the role of negative charges in comparison to PKA effects, we investigated if phosphomimetic substitutions at each PKA-mediated phosphoserine affect C1-M-domain structure. Fig. 7A shows that Asp-for-Ser substitutions increase distances and FWHM to a similar extent as phosphorylation with no differences observed in the distance distribution plots between unphosphorylated 4SD and phosphorylated biosensor. This suggests that the charge associated with Asp-for-Ser substitutions is sufficient to elicit change in structural dynamics and that negative charge plays a key role in cMyBP-C phosphorylation mechanisms. These results support earlier structural findings reported by Previs et al., 2016 [23] using a 4SD version of mouse C0-C3. However, we note that effects on FRET Efficiencies indicate some detectable differences between phosphomimetic and phosphorylated C0-C2 exist. Fig. S6 shows that Asp-for-Ser substitutions similarly reduce FRET Efficiency but to only ~40% of that induced by kinase-mediated phosphorylation, suggesting an intermediate effect of charge compared to PKA treatment. The partial effect could be due to differences in the overall negative charges imparted by aspartic acids and phosphorylation. Four aspartic acid residues (4SD) give a net increase in negative charge of 4 as compared to covalently-bound phosphate groups, which yield 8 negative charges. Thus, negative charge can account for at least part of the effects of phosphorylation on cMyBP-C structural dynamics. The intermediate effect of phosphomimetic substitutions in cMyBP-C has also been observed for actin binding [49], suggesting that single negative charge of an aspartic acid alone does not necessarily recapitulate phosphorylation. Thus, while rigorous TR-FRET analyses using 3-exponentials in a single-Gaussian model for distance distributions of 4SD fully recapitulate PKA treatment of wild type biosensor (Fig. 7A), simple evaluation using 1-exponential lifetime ratios to generate FRET Efficiencies (Fig. S6) only partially recapitulate phosphorylation (see also *Supplemental Results*). Investigations of phosphorylation compared to phosphomimetic substitutions using additional probe sites in future studies will clarify how well negative charge recapitulates phosphorylation beyond the C1-M-domain region.

4.6. Effects of HCM mutant R282W in biosensor and pathophysiological implications

The HCM mutant R282W eliminates cMyBP-C phosphorylation at Ser284 and so its effects on the spatial positioning of Cys225.Cys330 and structural changes brought about by phosphorylation were examined. Fig. 7B and Fig. S6 show that the extent of PKA-induced reduction in FRET Efficiency is blunted, as expected. This may be due to reduced Ser284 phosphorylation (Fig. S4), a consequence we have previously reported using mass spectrometry [25] and/or changes in Cys225. Cys330 spatial positioning that affect PKA's ability to phosphorylate C0-

C2. Changes in the unphosphorylated structure (Fig. 7B) and FRET Efficiency (Fig. S6) suggest that R282W modifies the C1-M-domain structural dynamics by causing an increase in D-A probe proximity. This is supported by a significant reduction in Cys225.Cys330 distance and an increase in FRET Efficiency. Upon PKA treatment, the effect in R282W is reduced, which appear to be largely due to changes in Γ_j, with a 5.7% increase compared to 30.4% in biosensor, although changes in center distance are also observed. It is unclear whether the structural change in unphosphorylated R282W compared to wild type biosensor or the reduced PKA response of R282W is the primary driver to explain why phosphorylated R282W exhibits a similar distance distribution as unphosphorylated wild type. In any case, phosphorylated R282W distances and FRET Efficiencies do not reach the levels of phosphorylated wild type (Fig. 7B and Fig. S6), consistent with a reduced response. In conclusion, these findings suggest that the R282W mutation affects cMyBP-C N-terminal structure in both unphosphorylated and phosphorylated forms with potential implications on C0-C2 function. We previously reported that R282W reduced binding of C0-C2 to actin and actin-tropomyosin, which may be explained in part by changes in C0-C2 structure that modify actin-binding interfaces on C0-C2 [25]. Further studies using additional cysteine TR-FRET pairs will further illuminate the mechanism of R282W cMyBP-C in HCM.

4.7. Limitations and future directions

We have reported similar levels of percent change and *Z'*-factors in another lifetime-based assay [25] that was further optimized to screen for, and identify, the first small-molecule compounds that modulate the cMyBP-C-actin interaction [48]. Before screening a library of small-molecule compounds, similar optimization will be performed to maximize the effectiveness of C0-C2$^{Cys225.Cys330}$ as a HTS biosensor. Due to the shorter, higher energy wavelengths of the UV spectrum (blue) used to excite our donor probe, IAEDANS, our 355 nm laser will result in autofluoresce of some compounds [50,51]. Therefore, red-shifted dyes excited by either a 473 or 532 nm laser will be optimized for the C0-C2 biosensor for HTS.

Future studies using the C0-C2$^{Cys225.Cys330}$ biosensor described here will investigate dynamics in actomyosin bound states as well as the effects of key cMyBP-C HCM mutations, notably those localized in C1 and M-domains. Proof-of-concept studies in C0-C2-R282W$^{Cys225.Cys330}$ establish the feasibility of our FRET-based approach to identify compounds to restore HCM C0-C2 structural dynamics similar to biosensor control and provide a novel platform to evaluate HCM mutations affecting MyBP-C's molecular structure. PKA effects on the actin- or myosin-bound biosensor may result in new potential screens. Additionally, by introducing alternative cysteine positions into the C0-C2$^{Cys-free}$ construct, we can perform similar studies between and within different regions of human cardiac C0-C2. Though our initial attempts to add cysteines to C2 were unsuccessful, we have recently identified mutation sites amenable for producing soluble and intact mutant C0-C2 protein for labeling C2 in future studies. Using TR-FRET, we aim to improve the understanding of phosphorylation-dependent structural changes in cMyBP-C that mediate changes in contractility.

Finally, conclusions regarding PKA-mediated conformational changes will need to be tested in more physiological models. For this we anticipate utilizing in situ replacement of endogenous cMyBP-C with labeled cMyBP-C. Likewise, future compounds identified by HTS using the described biosensor will need to be further screened using lower throughput methods to determine if they have the desired effects on cMyBP-C modulated functions, such as actomyosin binding (by cosedimentation), regulation of myofilament rotational dynamics (by transient phosphorescence anisotropy), myosin ATPase, and force development kinetics in skinned myocardial preparations.

4.8. Conclusions

A functional and effective human N-terminal cMyBP-C TR-FRET biosensor, C0-C2$^{Cys225.Cys330}$, has been identified for use in measuring phosphorylation- and mutation-mediated changes in protein structural dynamics for use in HTS and mechanistic studies.

Declaration of Competing Interest

B.A.C. serves as President of BC Biologics LLC. This relationship has been reviewed and managed by the University of Arizona. BC Biologics had no role in this study. B.A. Colson and R.-S. Kanassatega filed a PCT patent application based on this work (patent pending, serial no. PCT/US21/049836). The other authors declare no competing financial interests.

Acknowledgements

This work was supported by NIH grants R01 HL141564 (to B.A.C.) and T32 HL007249 (to C. Gregorio and J. Konhilas, University of Arizona) and an American Heart Association Predoctoral Fellowship (to R. K.)

Appendix A. Supplementary data

Supplementary data to this article can be found online at https://doi.org/10.1016/j.yjmcc.2022.02.005.

References

[1] P.K. Luther, et al., Understanding the organisation and role of myosin binding protein C in normal striated muscle by comparison with MyBP-C knockout cardiac muscle, J. Mol. Biol. 384 (1) (2008) 60–72.
[2] R. Craig, G. Offer, The location of C-protein in rabbit skeletal muscle, Proc. R. Soc. Lond. B Biol. Sci. 192 (1109) (1976) 451–461.
[3] P. Tonino, et al., Fine mapping titin's C-zone: matching cardiac myosin-binding protein C stripes with titin's super-repeats, J. Mol. Cell. Cardiol. 133 (2019) 47–56.
[4] L. Carrier, et al., Organization and sequence of human cardiac myosin binding protein C gene (MYBPC3) and identification of mutations predicted to produce truncated proteins in familial hypertrophic cardiomyopathy, Circ. Res. 80 (3) (1997) 427–434.
[5] M. Gautel, et al., Phosphorylation switches specific for the cardiac isoform of myosin binding protein-C: a modulator of cardiac contraction? EMBO J. 14 (9) (1995) 1952–1960.
[6] T. Okagaki, et al., The major myosin-binding domain of skeletal muscle MyBP-C (C protein) resides in the COOH-terminal, immunoglobulin C2 motif, J. Cell Biol. 123 (3) (1993) 619–626.
[7] C. Moos, et al., Interaction of C-protein with myosin, myosin rod and light meromyosin, J. Mol. Biol. 97 (1) (1975) 1–9.
[8] G. Offer, C. Moos, R. Starr, A new protein of the thick filaments of vertebrate skeletal myofibrils. Extractions, purification and characterization, J. Mol. Biol. 74 (4) (1973) 653–676.
[9] A. Freiburg, M. Gautel, A molecular map of the interactions between titin and myosin-binding protein C. implications for sarcomeric assembly in familial hypertrophic cardiomyopathy, Eur. J. Biochem. 235 (1–2) (1996) 317–323.
[10] D.O. Furst, U. Vinkemeier, K. Weber, Mammalian skeletal muscle C-protein: purification from bovine muscle, binding to titin and the characterization of a full-length human cDNA, J. Cell Sci. 102 (Pt 4) (1992) 769–778.
[11] K. Lee, et al., Orientation of myosin binding protein C in the cardiac muscle sarcomere determined by domain-specific immuno-EM, J. Mol. Biol. 427 (2) (2015) 274–286.
[12] S. Rahmanseresht, et al., The N terminus of myosin-binding protein C extends toward actin filaments in intact cardiac muscle, J. Gen. Physiol. 153 (3) (2021).
[13] M. Gruen, H. Prinz, M. Gautel, cAPK-phosphorylation controls the interaction of the regulatory domain of cardiac myosin binding protein C with myosin-S2 in an on-off fashion, FEBS Lett. 453 (3) (1999) 254–259.
[14] J. Ratti, et al., Structure and interactions of myosin-binding protein C domain C0: cardiac-specific regulation of myosin at its neck? J. Biol. Chem. 286 (14) (2011) 12650–12658.
[15] J.Y. Mun, et al., The cMyBP-C HCM variant L348P enhances thin filament activation through an increased shift in tropomyosin position, J. Mol. Cell. Cardiol. 91 (2016) 141–147.
[16] C. Risi, et al., N-terminal domains of cardiac myosin binding protein C cooperatively activate the thin filament, Structure 26 (12) (2018) 1604–1611 e4.
[17] J.M. Squire, P.K. Luther, C. Knupp, Structural evidence for the interaction of C-protein (MyBP-C) with actin and sequence identification of a possible actin-binding domain, J. Mol. Biol. 331 (3) (2003) 713–724.

[18] P.C. Rosas, et al., Phosphorylation of cardiac myosin-binding protein-C is a critical mediator of diastolic function, Circ. Heart Fail. 8 (3) (2015) 582–594.
[19] J.E. Stelzer, J.R. Patel, R.L. Moss, Protein kinase A-mediated acceleration of the stretch activation response in murine skinned myocardium is eliminated by ablation of cMyBP-C, Circ. Res. 99 (8) (2006) 884–890.
[20] H.C. Hartzell, Phosphorylation of C-protein in intact amphibian cardiac muscle. Correlation between 32P incorporation and twitch relaxation, J. Gen. Physiol. 83 (4) (1984) 563–588.
[21] L.M. Hanft, et al., Molecule specific effects of PKA-mediated phosphorylation on rat isolated heart and cardiac myofibrillar function, Arch. Biochem. Biophys. 601 (2016) 22–31.
[22] B.A. Colson, et al., Myosin binding protein-C phosphorylation is the principal mediator of protein kinase a effects on thick filament structure in myocardium, J. Mol. Cell. Cardiol. 53 (5) (2012) 609–616.
[23] M.J. Previs, et al., Phosphorylation and calcium antagonistically tune myosin-binding protein C's structure and function, Proc. Natl. Acad. Sci. U. S. A. 113 (12) (2016) 3239–3244.
[24] H.C. Hartzell, L. Titus, Effects of cholinergic and adrenergic agonists on phosphorylation of a 165,000-Dalton myofibrillar protein in intact cardiac muscle, J. Biol. Chem. 257 (4) (1982) 2111–2120.
[25] T.A. Bunch, et al., A high-throughput fluorescence lifetime-based assay to detect binding of myosin-binding protein C to F-actin, J. Gen. Physiol. 153 (3) (2021).
[26] J.W. McNamara, R.R. Singh, S. Sadayappan, Cardiac myosin binding protein-C phosphorylation regulates the super-relaxed state of myosin, Proc. Natl. Acad. Sci. U. S. A. 116 (24) (2019) 11731–11736.
[27] J.F. Shaffer, R.W. Kensler, S.P. Harris, The myosin-binding protein C motif binds to F-actin in a phosphorylation-sensitive manner, J. Biol. Chem. 284 (18) (2009) 12318–12327.
[28] R. Yamasaki, et al., Protein kinase a phosphorylates titin's cardiac-specific N2B domain and reduces passive tension in rat cardiac myocytes, Circ. Res. 90 (11) (2002) 1181–1188.
[29] O. Copeland, et al., Analysis of cardiac myosin binding protein-C phosphorylation in human heart muscle, J. Mol. Cell. Cardiol. 49 (6) (2010) 1003–1011.
[30] C.W. Tong, et al., Acceleration of crossbridge kinetics by protein kinase a phosphorylation of cardiac myosin binding protein C modulates cardiac function, Circ. Res. 103 (9) (2008) 974–982.
[31] A. El-Armouche, et al., Molecular determinants of altered Ca2+ handling in human chronic atrial fibrillation, Circulation 114 (7) (2006) 670–680.
[32] A. El-Armouche, et al., Decreased phosphorylation levels of cardiac myosin-binding protein-C in human and experimental heart failure, J. Mol. Cell. Cardiol. 43 (2) (2007) 223–229.
[33] A.M. Jacques, et al., Myosin binding protein C phosphorylation in normal, hypertrophic and failing human heart muscle, J. Mol. Cell. Cardiol. 45 (2) (2008) 209–216.
[34] S. Sadayappan, et al., Cardiac myosin binding protein C phosphorylation is cardioprotective, Proc. Natl. Acad. Sci. U. S. A. 103 (45) (2006) 16918–16923.
[35] P.C. Rosas, et al., Cardiac myosin binding protein-C phosphorylation mitigates age-related cardiac dysfunction: Hope for better aging? JACC Basic Transl. Sci. 4 (7) (2019) 817–830.
[36] L.M. Hanft, C.A. Emter, K.S. McDonald, Cardiac myofibrillar contractile properties during the progression from hypertension to decompensated heart failure, Am. J. Physiol. Heart Circ. Physiol. 313 (1) (2017) H103–H113.
[37] W. Jia, et al., Identification of novel protein kinase A phosphorylation sites in the M-domain of human and murine cardiac myosin binding protein-C using mass spectrometry analysis, J. Proteome Res. 9 (4) (2010) 1843–1853.
[38] J.W. Howarth, et al., Structural insight into unique cardiac myosin-binding protein-C motif: a partially folded domain, J. Biol. Chem. 287 (11) (2012) 8254–8262.
[39] B.A. Colson, et al., Site-directed spectroscopy of cardiac myosin-binding protein C reveals effects of phosphorylation on protein structural dynamics, Proc. Natl. Acad. Sci. U. S. A. 113 (12) (2016) 3233–3238.
[40] J. Erdmann, et al., Spectrum of clinical phenotypes and gene variants in cardiac myosin-binding protein C mutation carriers with hypertrophic cardiomyopathy, J. Am. Coll. Cardiol. 38 (2) (2001) 322–330.
[41] T.A. Bunch, et al., N-terminal extension in cardiac myosin-binding protein C regulates myofilament binding, J. Mol. Cell. Cardiol. 125 (2018) 140–148.
[42] T.A. Bunch, et al., Human cardiac myosin-binding protein C restricts actin structural dynamics in a cooperative and phosphorylation-sensitive manner, J. Biol. Chem. 294 (44) (2019) 16228–16240.
[43] C. Louis-Jeune, M.A. Andrade-Navarro, C. Perez-Iratxeta, Prediction of protein secondary structure from circular dichroism using theoretically derived spectra, Proteins 80 (2) (2012) 374–381.
[44] J.M. Muretta, et al., High-performance time-resolved fluorescence by direct waveform recording, Rev. Sci. Instrum. 81 (10) (2010), 103101.
[45] J.H. Zhang, T.D. Chung, K.R. Oldenburg, A simple statistical parameter for use in evaluation and validation of high throughput screening assays, J. Biomol. Screen. 4 (2) (1999) 67–73.
[46] A.V. Inchingolo, et al., Revealing the mechanism of how cardiac myosin-binding protein C N-terminal fragments sensitize thin filaments for myosin binding, Proc. Natl. Acad. Sci. U. S. A. 116 (14) (2019) 6828–6835.
[47] S. Nag, et al., The myosin mesa and the basis of hypercontractility caused by hypertrophic cardiomyopathy mutations, Nat. Struct. Mol. Biol. 24 (6) (2017) 525–533.
[48] T.A. Bunch, et al., Cardiac myosin-binding protein C interaction with actin is inhibited by compounds identified in a high-throughput fluorescence lifetime screen, J. Biol. Chem. 297 (1) (2021), 100840 (1-12).
[49] T. Kampourakis, et al., Structural and functional effects of myosin-binding protein-C phosphorylation in heart muscle are not mimicked by serine-to-aspartate substitutions, J. Biol. Chem. 293 (37) (2018) 14270–14275.
[50] T.M. Schaaf, et al., Red-shifted FRET biosensors for high-throughput fluorescence lifetime screening, Biosensors (Basel) 8 (4) (2018).
[51] A. Simeonov, et al., Fluorescence spectroscopic profiling of compound libraries, J. Med. Chem. 51 (8) (2008) 2363–2371.